Influence of Capacitive Transducer Nonlinearities on the Amplitude Limiting of MEMS Based Oscillators

Sherwin Afshar

Electrical Engineering and Computer Sciences
University of California, Berkeley

Technical Report No. UCB/EECS-2022-227
http://www2.eecs.berkeley.edu/Pubs/TechRpts/2022/EECS-2022-227.html

September 12, 2022

Influence of Capacitive Transducer Nonlinearities on the Amplitude Limiting of MEMS Based Oscillators

by Sherwin Afshar

Research Project

Submitted to the Department of Electrical Engineering and Computer Sciences, University of California at Berkeley, in partial satisfaction of the requirements for the degree of **Master of Science, Plan II**.

Approval for the Report and Comprehensive Examination:

Committee:

Professor Clark Nguyen
Research Advisor

8/12/22

(Date)

* * * * * * *

Professor Kris Pister
Second Reader

August 12, 2022

(Date)

Acknowledgements

I would like to thank Qianyi Xie for teaching me everything I know about measuring MEMS resonators in probe station, wire bonding, testing oscillators, and releasing dies. I would also like to thank Kevin Zheng for all the help and support with taping out, and making sure the lab stays polished. Also, I want to thank Qiutong Jin for dropping all the dies I've released into CPD in the Nanolabs for me. Furthermore, I want to thank Clark Nguyen for bringing me into MEMS research when I was a sophomore undergrad. Finally, I want to thank my family for all the support throughout my education and life.

Contents

Chapter 1

Introduction

Micro electromechanical system (MEMS) based oscillators have become crucial for RF systems requiring high performing references with minimal power consumption. The combination of higher quality factor and low parasitic capacitances allows them to out-perform typical quartz crystal oscillators, capable of working at higher frequencies while providing excellent frequency stability with little power consumption. Previous work in [1] has demonstrated a 61 MHz oscillator meeting the GSM phase noise specification, while consuming less than 80 μW of power. More recent work in [2] demonstrates a 199 MHz oscillator, which is a much higher frequency than the limit for quartz crystal resonators, which is around 60 MHz.

The key enabler for scaling capacitive transducer MEMS up in frequency while consuming less power is reducing the electrode-to-structure air gap, which drastically lowers the series motional resistance. As the transducer gap gets reduced further to improve performance of oscillators, it becomes more important to understand the nonlinearities which come with it. Lumped electrical models suffice for small signal analysis, but fall short of predicting the performance of oscillators reference to “tiny gap” resonators. This work aims to model the transducer nonlinearities of MEMS resonators, and apply the analysis to explain differences in the amplitude limiting of MEMS based oscillators from crystal based ones.

Chapter 2

Linear Modeling of the Wineglass Disk Resonator

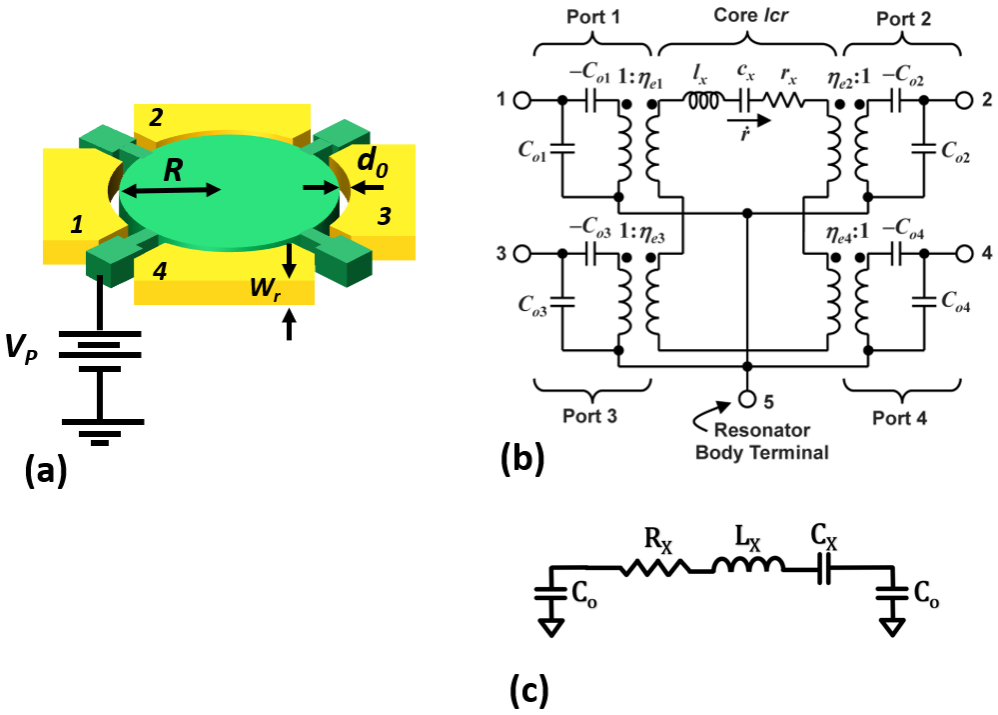

Figure 1: Side supported wineglass disk resonator (a), equivalent circuit model (right)

Capacitive transducer MEMS resonators can be modeled as a high Q series resonant LCR tank with an ideal transformer which models the electro-mechanical coupling factor. Figure 1 shows a side supported disk resonator with four electrodes, designed to operate in the wineglass mode. The core LCR represent the lumped mass, stiffness, and damping of the mechanical structure, can be derived from the equations below for the wineglass mode [3].

$$l_X = m_m = \chi M_{tot} = \chi \rho \pi R^2 W_r$$

$$c_x = \frac{1}{k_m} = \frac{1}{\omega_{nom}^2 m_m}$$

$$r_x = b_m = \frac{\sqrt{k_m m_m}}{Q}$$

Where $\chi = 0.967$ is the mode shape coefficient for the wineglass mode, ρ is the density of polysilicon, R is the radius of the disk, and W_r is the thickness of the disk.

The ideal transformer models the electro-mechanical coupling, where the turn ratio is given by the equation:

$$\eta_e = \frac{V_p k_i C_o}{d_o} = \frac{V_p k_i \epsilon_o A_{ovlp}}{d_o^2}$$

V_P is the bias voltage of the structure, C_0 is the electrode capacitance to the structure, d_o is the structure to electrode air gap, A_{ovlp} is the electrode to structure overlap area, and $k_i = 0.724$ for the wineglass mode. In the wineglass mode, the current through ports 1 and 3 are in phase with each other, which are 180 degrees out of phase with ports 2 and 4. Connecting the ports that are in phase to each other gives the electrical model in Figure 1c, where:

$$R_x = \frac{r_x}{4\eta_e^2}, L_x = \frac{l_x}{4\eta_e^2}, C_x = 4\eta_e^2 c_x \,//\, (-2C_o)$$

Chapter 3

The Pierce Oscillator

3.1 Small Signal Theory of the Pierce Oscillator

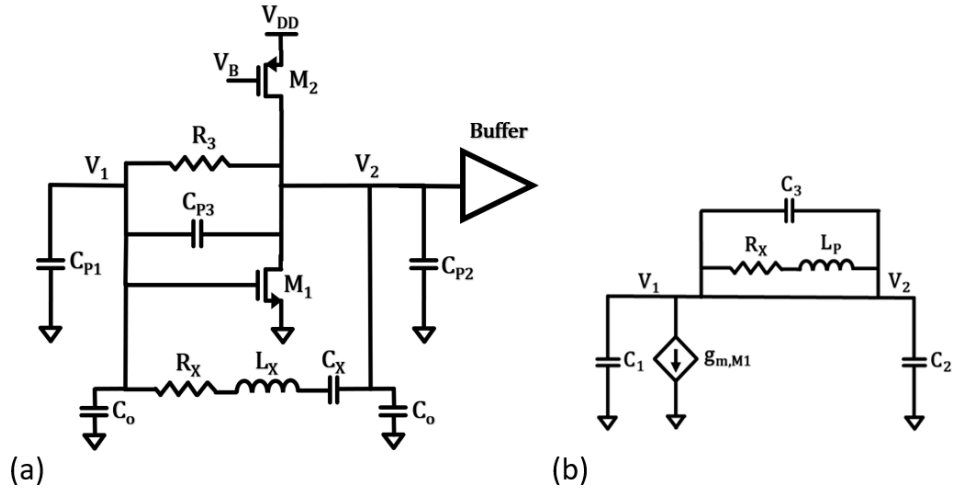

Figure 2: (a) Pierce oscillator schematic and (b) small signal equivalent operating at parallel resonance

The pierce oscillator is commonly used for quartz crystal resonators, and has proven to have great performance as a MEMS based oscillator as well. The theory of the MEMS based pierce oscillator is identical to that of a crystal. The main difference is the series motional resistance, R_x, of the MEMS resonator is often much larger than a crystal, but the MEMS based oscillator has much lower parasitic capacitances, C_1, C_2, and C_3, allowing it to consume less power. The output impedances of M1 and M2 can be ignored, as they are typically much greater than the impedance of C_1 and C_2 at the oscillation frequency.

In order to meet a loop phase of 0 degrees for oscillation start up, the resonator has to operate in parallel resonance, and can be modeled as a series LR network, where:

$$L_P = \frac{1}{\omega_o^2(C_3 + C_1//C_2)}$$

ω_0 is the series resonant frequency. For a high Q resonator, the frequency pulling from operating at parallel resonance can be ignored for the purpose oscillation startup analysis. Breaking the loop at the gate of M1, the loop gain can be formulated as:

$$A_L = -\frac{g_m}{C_1 + C_2}\frac{1}{s(s^2 L_p C_p + sR_x C_p + 1}$$

$$where\ C_p = C_1//C_2 + C_3$$

The critical g_m for oscillation can be solved by setting the loop gain to unity, giving

$$g_{m,crit} = C_1 C_2 \omega_o^2 \left(1 + \frac{C_1 + C_2}{C_1 C_2} C_3\right)^2 R_X$$

$$assuming \quad g_{m1} C_3 \ll \omega_o (C_1 C_2 + C_1 C_3 + C_2 C_3)$$

From the analysis, we can see the importance of minimizing R_x. Assuming the bias current of M1 is proportional to $g_{m1} = \frac{2I_D}{V^*}$, we can see the power consumption of the pierce has a fourth power dependence on the capacitive transducer gap.

$$P_{pierce} = \frac{V_{DD} V^*}{2} C_1 C_2 \omega_o^2 \left(1 + \frac{C_1 + C_2}{C_1 C_2} C_3\right)^2 \frac{r_x d_o^4}{4(V_p k_i \epsilon_o A_{ovlp})^2}$$

This highlights the importance of scaling down the transducer gap, and understanding the nonlinearities which come with it.

3.2 Pierce Oscillator Design

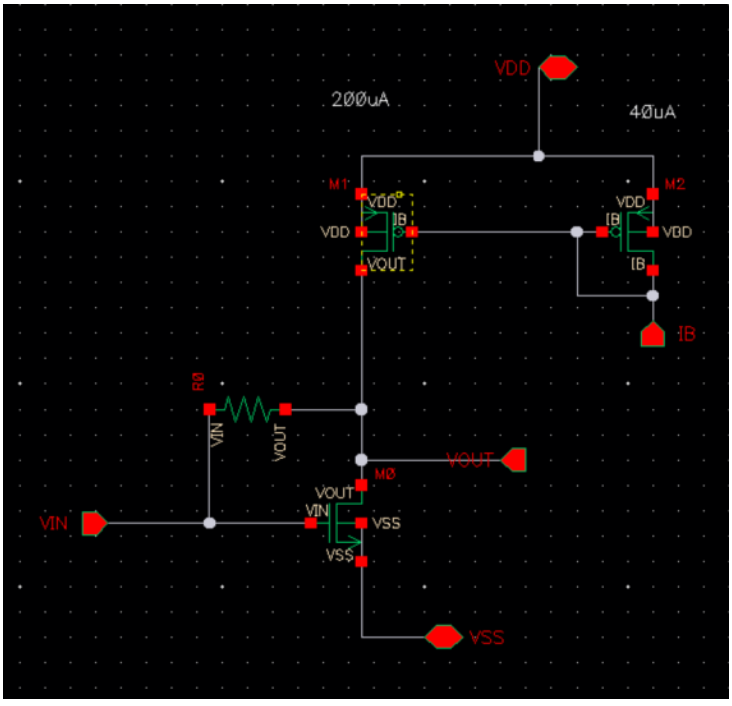

Figure 3: Pierce oscillator designed in TSMC 180nm

M0	36u / .36u
M1	25.6u / 1u
M2	6.4u / 1u
R0	100k

Table 1: Device and passive sizings for the pierce oscillator

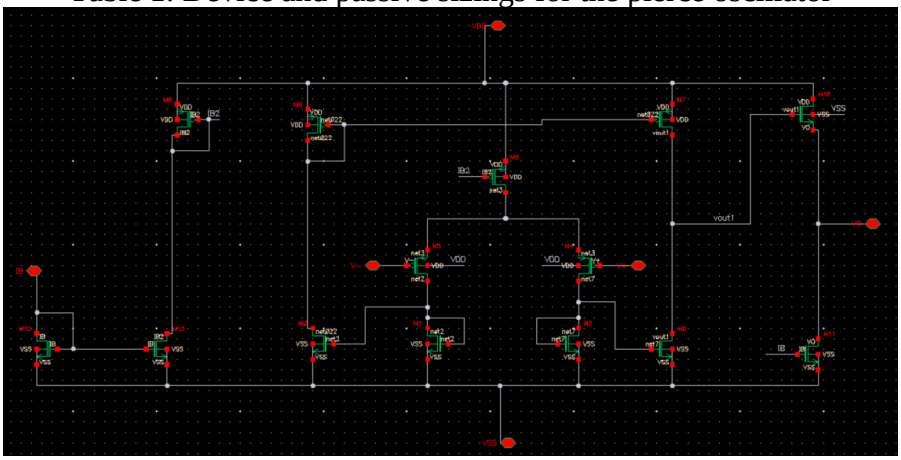

Figure 4: Current mirror op-amp with common drain output stage for the closed loop buffer

A pierce oscillator was taped out in TSMC 180nm. Figure 3 shows the pierce sustaining amplifier, with device sizings given in Table 1. Theory on phase noise highlighted in [1] described how *1/f* noise from the active load and g_m device contribute to $1/f^3$ phase noise. Using longer channel lengths is an effective method to improve phase noise performance of the oscillator. To minimize power consumption, it is important for the buffer to have minimal input capacitance, while capable of driving 50Ω terminated coax lines at the maximum oscillation amplitude, around 500 mV. The current mirror op-amp provided excellent linearity, needed for oscillation amplitude measurements, with a design GBW of 700 MHz.

3.3 Fully Differential Pierce Oscillator Design

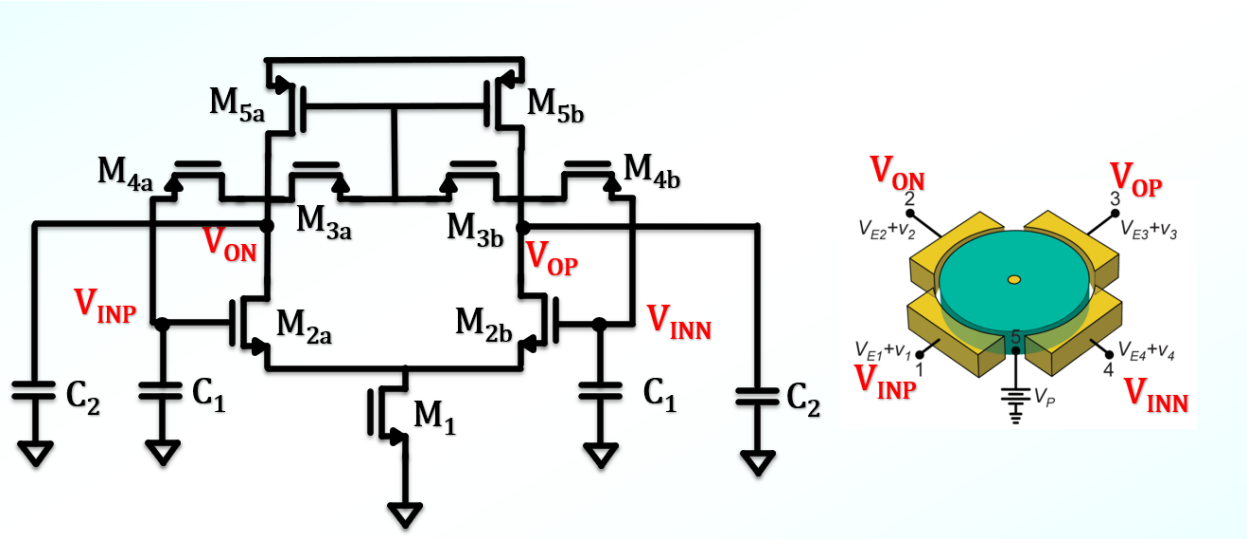

Figure 5: Fully Differential Pierce Oscillator

Another version of the pierce topology is the fully differential, using a differential pair with resistive common mode feedback as the g_m stage of the pierce. The analysis is almost identical to the single-ended pierce in Figure 2b, with the single ended small signal parameters replaced with their differential counterparts: $G_{m,d} = g_{m2}, C_{1,D} = \frac{1}{2}C_1,\ C_{2,D} = \frac{1}{2}C_2,\ R_{x,D} = R_x$

The circuit has been taped out in TSMC 180nm, with the device sizings shown in Table 2

M1	105.92u / 600n
M2	15.68u / 180n
M3	29.92u / 180n
M4	29.92u / 180n
M5	64u / 400n

Table 2: Device sizings for fully differential TIA design

Chapter 4
Amplitude Limiting of the Pierce Oscillator

4.1 Theory

As we will see in the following sections, nonlinearities of small gap MEMS resonators affects the amplitude limiting of the pierce oscillator. To understand how, analysis and experimentation has been conducted on the amplitude limiting of quartz crystal oscillators, and applied to MEMS based oscillators, assuming an ideal, linear resonator.

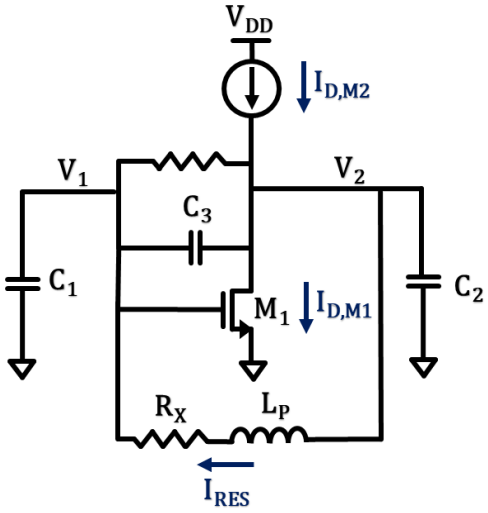

Figure 6: Large signal model of the pierce oscillator

Analysis on the amplitude limiting of the pierce oscillator has been done in [5], and a similar approach has been taken in this work. A key difference is the influence of larger R_x on the relative waveforms of the pierce. In quartz crystal oscillators, V_1 and V_2 are perfectly 180 degrees out of phase with each other, with a transfer function of $\frac{V_1}{V_2} = -\frac{C_2}{C_1}$, which neglects the influence of series motional resistance. This is a good approximation for crystal oscillators, since crystal resonators have much smaller motional resistances, but R_X must be taken in account when analyzing the amplitude limiting of MEMS oscillators. In the same fashion, the transfer function describing the relative waveforms at V_1 and V_2 is written in the equation below, including the effect of R_X and C_3.

$$\frac{V_1}{V_2} = \frac{(j\omega)^2 L_P C_3 + (j\omega) R_X C_3 + 1}{(j\omega)^2 L_P (C_1 + C_3) + (j\omega) R_X (C_1 + C_3)}$$

After substituting L_p for the quantity written in terms of capacitances, we get the equation in a form which resembles a transfer function with a LHP zero and RHP pole.

$$\frac{V_1}{V_2} = -\frac{C_2}{C_1}\frac{1 + j\frac{\omega_o}{\omega_z}}{1 - j\frac{\omega_o}{\omega_p}}$$

$$\omega_z = \frac{C_1 C_2}{R_X C_3 (C_1 C_2 + C_1 C_3 + C_2 C_3)}$$

$$\omega_p = \frac{C_1^2}{R_X (C_1 + C_3)(C_1 C_2 + C_1 C_3 + C_2 C_3)}$$

One observation is that the effect of the numerator from ω_z can be ignored, since in a functioning pierce oscillator $C_1 >> C_3$. Given the previous assumption, the relative amplitudes and phase between V_1 and V_2 can be formulated:

$$A = \frac{C_2}{C_1}\frac{1}{\sqrt{1 + \left(\frac{\omega_o}{\omega_p}\right)^2}}$$

$$\phi = -tan^{-1}(\frac{\omega_o}{\omega_p})$$

From the analysis, we can see that when $\omega_0 \ll \omega_p$, the relative waveforms are identical the approximation in [5]. As ω_0 approaches ω_p, there is an additional attention and phase shift between V_1 and V_2.

Using the relative waveforms, the large signal waveform of V_1 and V_2 can be appropximated as

$$V_2 = V_B + V_o \cos(\omega_o t)$$

$$V_1 = V_B - \frac{C_2}{C_1} A V_o \cos(\omega_o t + \phi)$$

Where V_B is the periodic steady state DC component of the output voltages, and is strictly lower than the DC operating point of the sustaining amplifier. V_B can be solved by assuming an ideal current source as the active load, and imposing the condition that the average current through M1 must be equivalent to the DC current supplied by M2.

$$I_{D,M2} = \frac{1}{2\pi}\int_{-\pi}^{\pi} I_{D,M1} d\omega_o t$$

Where $I_{D,M1}$ is strictly a function of V_1, ignoring channel length modulation. To solve for V_o of the oscillator, the effective large signal transconductance must be derived as a function of V_o.

$$G_m = \frac{I_{D,M1(1)}}{V_{1(1)}} = \frac{C_1}{C_2 A V_o} I_{D,M1(1)}$$

$I_{D,M1(1)}$ is the first harmonic of the current through M1, and can be derived from a Fourier analysis.

The analytical large signal transconductance profile for the single ended pierce designed in Section X.X is plotted in Figure 7. As expected, G_m is equivalent to the small signal g_m of M1, and begins to drop more rapidly when M1 exits saturation for a portion of each period, with better linearity when operated at a larger V_{ov}.

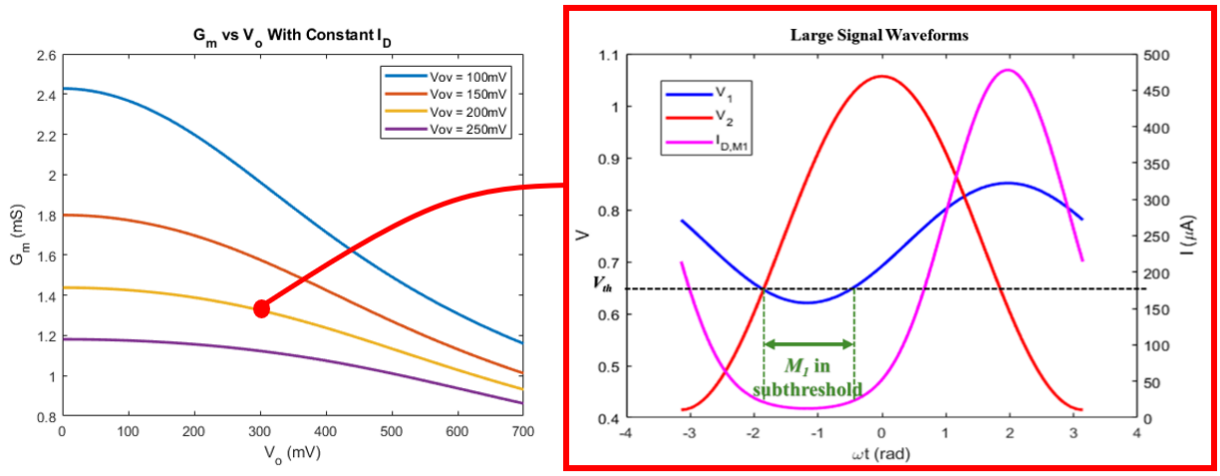

Figure 7: Large signal Gm versus Vo (left) with example waveforms (right) of the pierce operating at V_{ov} = 200mV and V_o = 300 mV

In steady state, the RHP complex pole of the oscillator are on the $j\omega$ axis, which means the output amplitude, V_o, is the solution to $G_m(V_o) = g_{m,crit}$. Visually, this is the intersection between $g_{m,crtt}$ and $G_m(V_o)$, with an example shown in Figure 8.

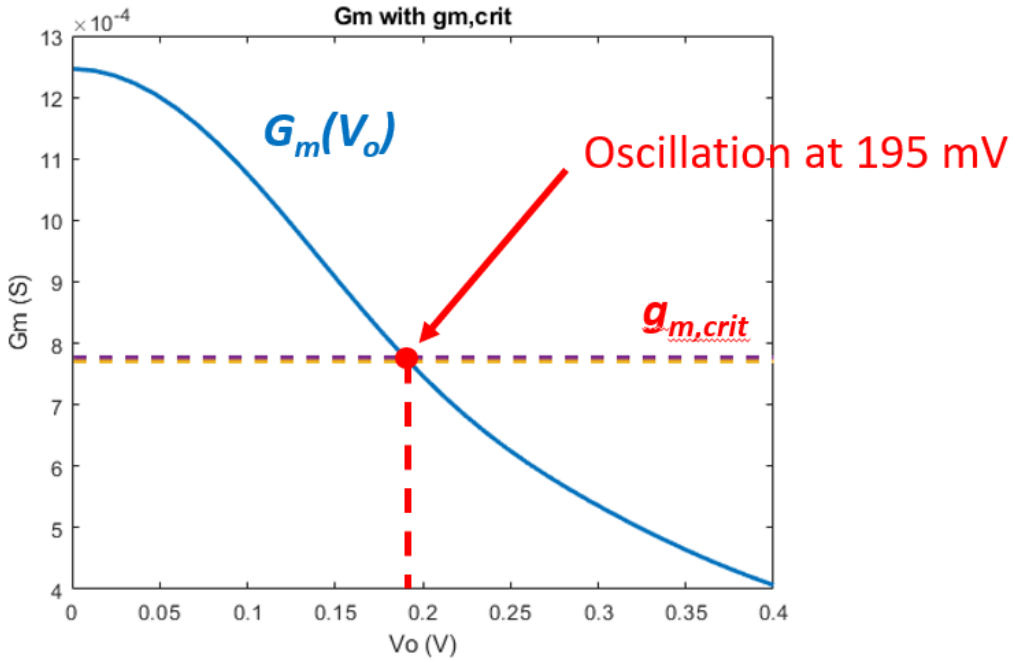

Figure 8: Visualization of solving for output amplitude of the pierce oscillator

The G_m nonlinearity is not the only mechanism which could limit the amplitude of oscillation. However, for moderately large amplitudes, where the active load does not exit saturation, it is the dominant nonlinearity limiting the amplitude of oscillation.

4.2 Experiment

To test the theory on amplitude limiting and relative waveforms in the pierce with larger R_x, an quartz crystal pierce oscillator was constructed using a resistor in series with the crystal to mimic a linear MEMS resonator with non-negligent R_x. The sustaining amplifier used was the same as [1]. Figure 9 shows the schematic and PCB of the experiment. The parasitics of the crystal were measured with a network analyzer, shown in Figure 10. The output amplitude of the oscillator is changed by sweeping the bias current of the pierce.

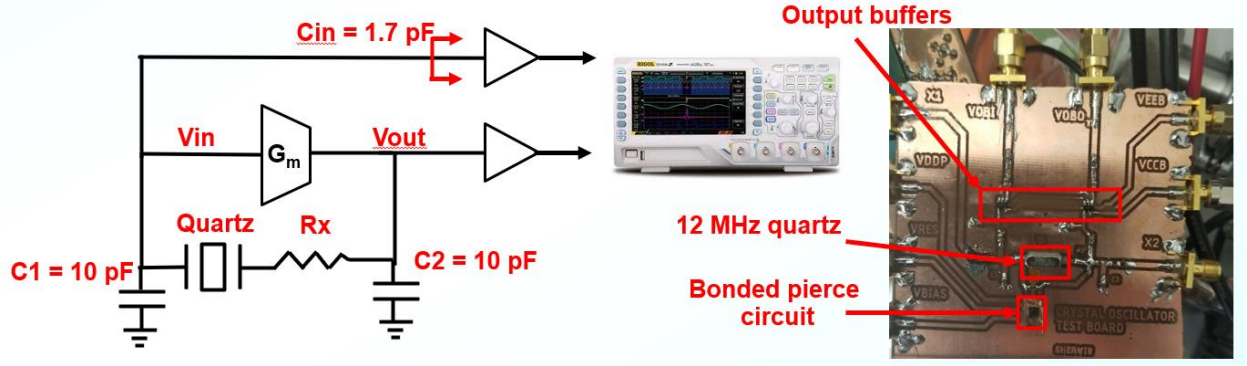

Figure 9: Schematic and PCB of the experiment to predict the amplitude and relative waveforms of a pierce

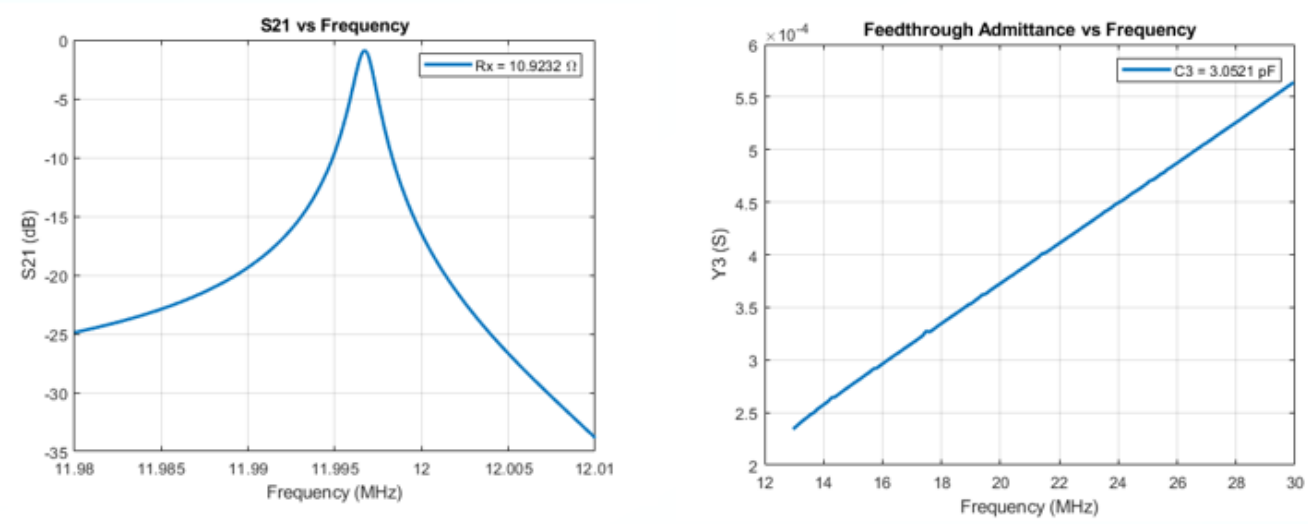

Figure 10: S21 measurement of the 12 MHz quartz crystal

Table 3 shows the nominal values of each passive in the schematic, along with the adjusted value within the error margin of the experiment which yielded a closer result to the theory. Figures 11 and 12 compare the theory of the input and output amplitudes, respectively, of the pierce. Table 4 compares the measured relative waveform magnitude and phase between the input and output voltage waveforms.

Component	Nominal Value	Adjusted Value
R_X	480 Ω, 700 Ω, 830 Ω, 1010 Ω	540Ω, 720Ω, 835Ω, 965Ω
C_1	11.7 pF	10.4 pF
C_2	11.7 pF	12 pF
C_3	3 pF	3 pF

Table 3: Passive component/parasitic values in the pierce oscillator

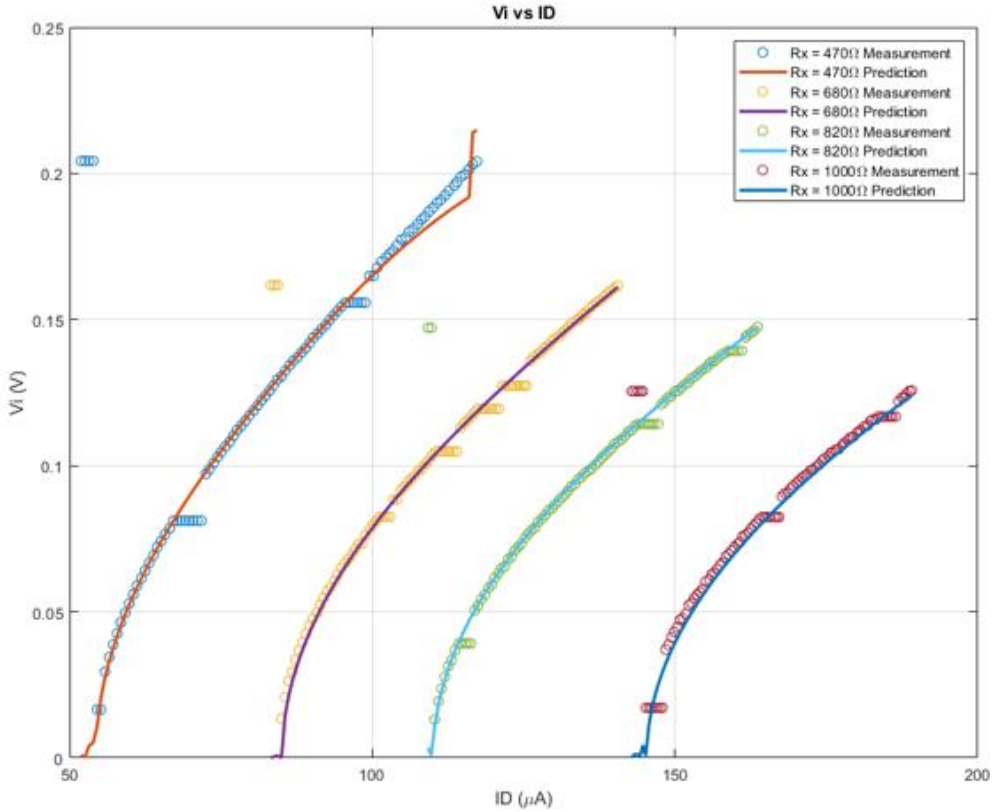

Figure 11: Amplitude at the input node of the pierce oscillator, prediction plotted with the measurement points.

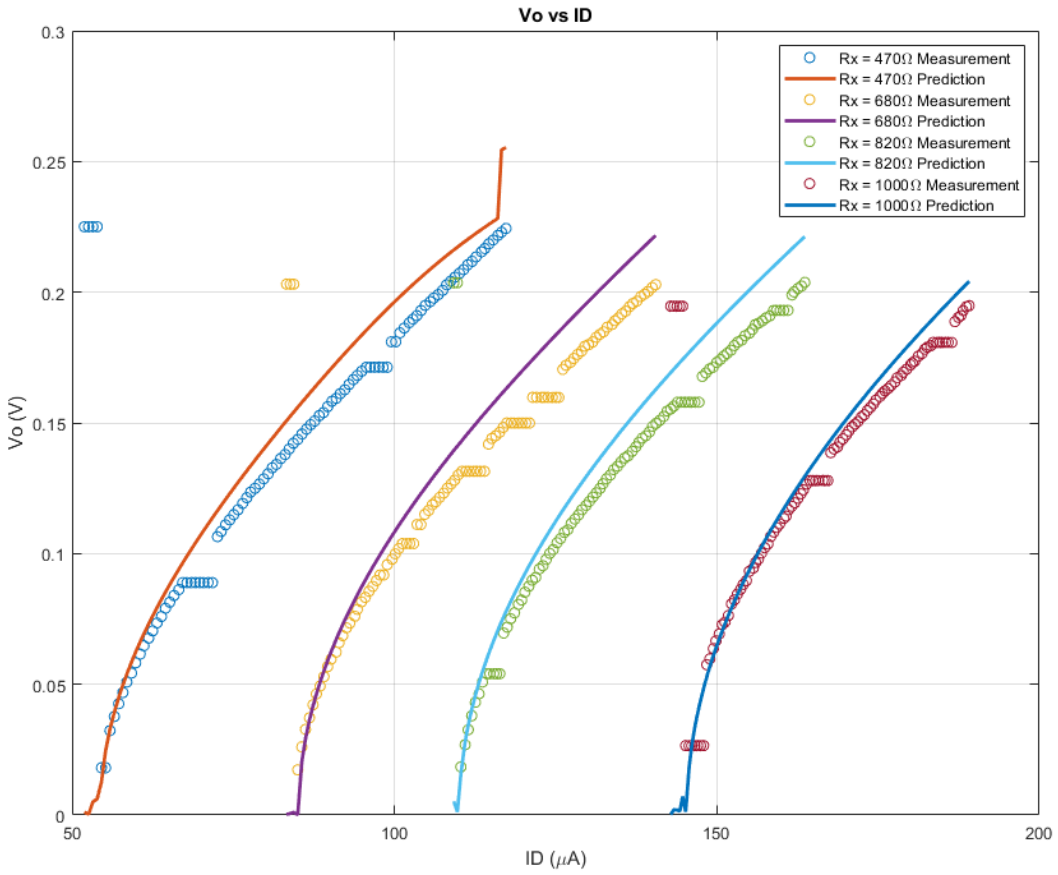

Figure 11: Amplitude at the output node of the pierce oscillator, prediction plotted with the measurement points.

Mag(Vi / Vo)

Rx	Measured	Calculated
470 Ω	0.91	0.84
680 Ω	0.8	0.73
820 Ω	0.72	0.67
1000 Ω	0.65	0.61

Phase(Vi / Vo) + 180°

Rx	Measured	Calculated
470 Ω	41.1°	44.0°
680 Ω	50°	52.2°
820 Ω	55°	56.2°
1000 Ω	60.0	60.0

Table 4: Measurement and calculation of the relative magnitude (left) and phase (right) between the input and output waveforms of the pierce.

From the experimental results, we can see that the large signal analysis does well at predicting the amplitude limiting of a pierce, when the resonator has good linearity and larger series motional resistance. Experimental results with an oscillator referenced to a 53 MHz wineglass disk resonator in Section X show very different behavior, and requires analysis of capacitive transducer nonlinearities.

Chapter 5

Capacitive Transducer Nonlinearities of Small Gap Resonators

5.1 Analysis

Dynamic nonlinearity in MEMS resonators have been analyzed in prior work, like in [4]. Transducer based spring softening and mechanical based spring stiffening leads to "duffing" in the frequency response, a phenomenon which has been analyzed and measured before for MEMS resonators. Figure 12, taken from [6], illustrates a duffing resonator under spring stiffening.

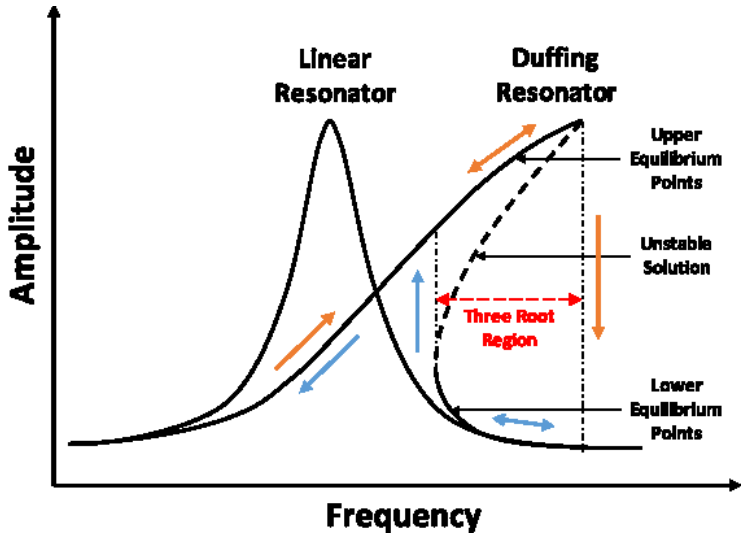

Figure 12: Illustration of a duffing resonator frequency response, taken from [6]

Duffing occurs due to dynamic nonlinearity in the resonator stiffness, which becomes a function of the displacement amplitude of the resonator, generally described by the equation $k_{tot} = k_m + k_{m2}(X)$. k_m is the small signal stiffness derived in Section 1, and k_{m2} represent the portion of the total stiff which is amplitude dependent. When k_{m2} term is positive, the stiffness increases with amplitude, making the frequency response bend to the right as the resonance frequency increases along with the displacement during a frequency sweep. The opposite is true for when the k_{m2} is negative.

As shown in the analysis ahead, spring softening is dominant for small gap MEMS resonators, and is the focus of the analysis. This work repeats the transducer nonlinear analysis similar to [4], applying it to small gap wineglass resonators instead. The following analysis also gives an explanation for gain expansion measured for small gap resonators, where the series motional resistance decreases at larger amplitudes.

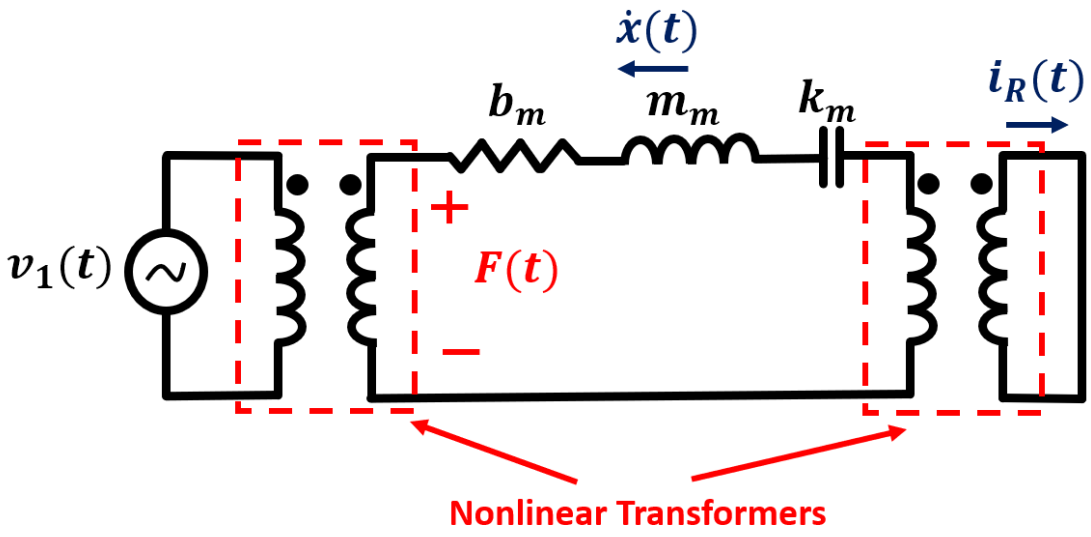

Figure 13: Nonlinear model of a capacitive transducer MEMS resonator used in analysis

The setup for the analysis is a wineglass disk resonator, with the in-phase ports connected to each other. To simplify the analysis, the mechanical nonlinearities of the resonator have been ignored, assuming a linear lumped mechanical model. Additionally, the displacement as a function of time is assumed to be sinusoidal, which is a reasonable assumption for high Q resonators.

The displacement, $x(t)$, and drive voltage, $v_1(t)$, can be written as

$$v_1(t) = 2V_1\cos(\omega t) = V_1 e^{j\omega t} + V_1^* e^{-j\omega t}$$

$$x_R(t) = 2X_R\cos(\omega t) = X_R e^{j\omega t} + X_R^* e^{-j\omega t}$$

Where V_1 and X_R can be complex. The factor of two is there to make the analysis simpler, and makes no difference in the end result. Not that this makes the solution, $|X_R|$, half the magnitude of the displacement amplitude. For a capacitive transducer, the force applied to the structure is

$$F(t) = \frac{1}{2}(V_P - v_1)^2\frac{\partial C}{\partial x} = \frac{1}{2}(V_P - v_1)^2\kappa_i\frac{C_0}{d_0}\left(1 - \kappa_i\frac{x}{d_0}\right)^{-2}$$

$$\approx \frac{1}{2}(V_P - v_1)^2\kappa_i\frac{C_0}{d_0}\left(1 + \frac{2\kappa_i}{d_0}x + \frac{3\kappa_i^2}{d_0^2}x^2 + \frac{4\kappa_i^3}{d_0^3}x^3\right)$$

The last expression substitutes $\left(1 - \kappa_i\frac{x}{d_0}\right)^{-2}$ for its Taylor expansion up to the third power, to model third order nonlinearity. After substituting the time function of v_1 and x_R and grouping all the terms at the fundamental frequency, and assuming $V_1 \ll V_P$ we get the expression:

$$F(t) = \left[-V_P V_1\kappa_i\frac{C_0}{d_0}V_1 - 6V_P V_1\kappa_i^3\frac{C_0}{d_0^3}|X_R|^2 + \left(V_P^2\kappa_i^2\frac{C_0}{d_0^2} + 6V_P^2\kappa_i^4\frac{C_0}{d_0^4}|X_R|^2\right)X_R\right]e^{j\omega t} + C.C.$$

Similar to solving for a linear system, the magnitude squared of the displacement, $|X_R|^2$, can be solved with the equation:

$$F = m_m\ddot{x} + b_m\dot{x} + k_m x$$

After substituting $x_R(t)$, we get

$$(-m_m\omega^2 X_R + j\omega b_m X_R + k_m X_R)e^{j\omega t} + C.C. = F(t)$$

Terms proportional to X_R in $F(t)$ can be treated as stiffness, since they represent a force proportional to displacement. Grouping them with the mechanical stiffness term, we get the full equation.

$$-m_m\omega^2 X_R + j\omega b_m X_R + (k_m - k_{e1} - k_{e2}|X_R|^2)X_R = (\eta_{e1} + \eta_{e2}|X_R|^2)V_1$$

$$k_{e1} = V_P^2\kappa_i^2\frac{C_0}{d_0^2} = \frac{\eta_{e1}^2}{C_0}, \qquad k_{e2} = 6V_P^2\kappa_i^4\frac{C_0}{d_0^4} = \frac{\eta_{e1}\eta_{e2}}{C_0}$$

$$\eta_{e1} = V_P\kappa_i\frac{C_0}{d_0}, \qquad \eta_{e2} = 6V_P\kappa_i^3\frac{C_0}{d_0^3}$$

Writing the equations in this form make it easier to understand the influence of small gap transducers on nonlinearity. The first observation is the term k_{e1} is the electrical stiffness, analyzed in [1], and comes from modeling $\frac{\partial C}{\partial x}$ up to the first order. η_{e1} is the linear transducer gain, seen in Section 1. Taking up to third order nonlinearity into account gives rise to amplitude dependent electrical stiffness, $k_{e2}|X_R|^2$, and transducer gain, $\eta_{e2}|X_R|^2$.

$i_R(t)$ can be solved from the solution of $|X_R|^2$ in a similar fashion, using the equation

$$i_R(t) = \frac{\partial C}{\partial x} = \dot{x}_R\kappa_i\frac{C_0}{d_0}(1 + \frac{2\kappa_i}{d_0}x_R + \frac{3\kappa_i^2}{d_0^2}x_R^2 + \frac{4\kappa_i^3}{d_0^3}x_R^3)$$

Substituting the sinusoidal form for x_R and grouping all terms at the fundamental frequency, we get the solution:

$$I_R = j\omega X_R(\eta_e + \eta_{e2}|X_R|^2)$$

Figure 14 shows the lumped model of a MEMS resonator taking transducer nonlinearity into account, and now has an amplitude dependent turn ratio and capacitance.

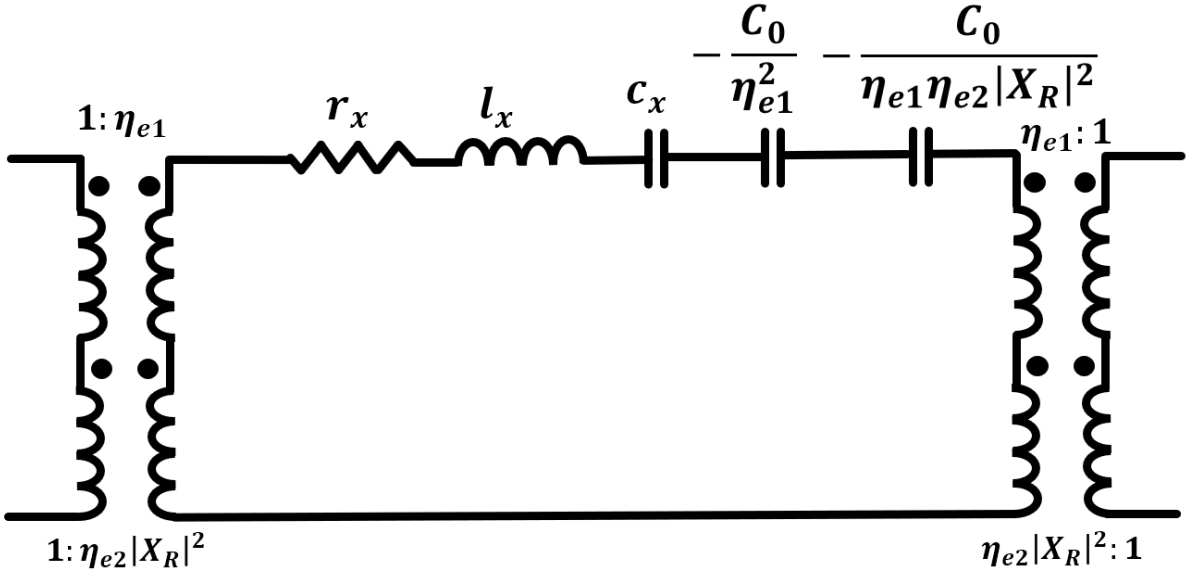

Figure 14: Lumped nonlinear model of a two port MEMS resonator

The amplitude dependent negative capacitance results in duffing when large enough, pulling the center resonance frequency lower than the nominal small signal center frequency. The amplitude dependent resonance frequency can be written as:

$$f_0 = \frac{1}{2\pi}\sqrt{\frac{k_m - \frac{\eta_{e1}^2}{C_0} - \frac{\eta_{e1}\eta_{e2}|X_R|^2}{C_0}}{m_m}}$$

Another effect is the reduction of series motional resistance with increasing amplitude, and can be written as

$$R_x = \frac{r_x}{(\eta_{e1} + \eta_{e2}|X_R|^2)^2}$$

5.2 Measurements

Figures 15, 16, and 17 shows the frequency response of a 40 nm gap 13 MHz, 27 MHz, and 53 MHz wineglass disk resonator respectively. The measurements were taken using a Lakeshore vacuum probing station, with a network analyzer. All three resonators are spring softening dominated, which is not necessarily the case with larger gap resonators. This is due to the strong dependence of nonlinear electrical stiffness on the gap, d_0. Additionally for moderately large input powers, we can see the admittance at peak resonance increase, consistent with the analysis showing R_X decreasing at larger amplitudes. At much larger input powers, however, the admittance at peak resonance takes the opposite trend, and decreases with increasing amplitude. This is possibly due to other mechanical nonlinearities, and cannot be explained by transducer nonlinearity alone.

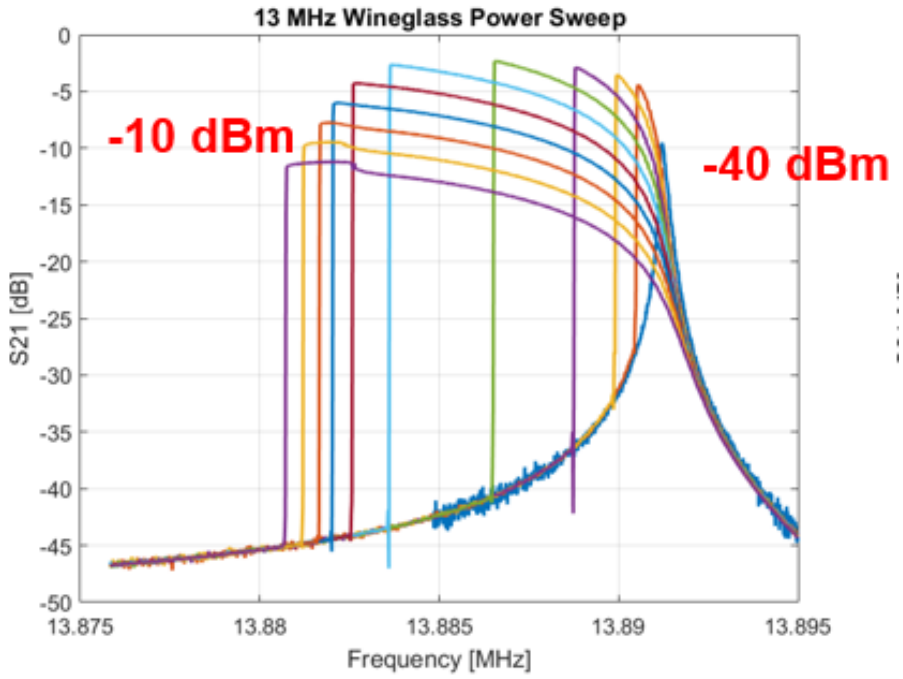

Figure 15: Frequency response of a 40 nm gap 13 MHz wineglass disk resonator, with V_P = 2 V, sweeping input power from -40 dBm to -10 dBm

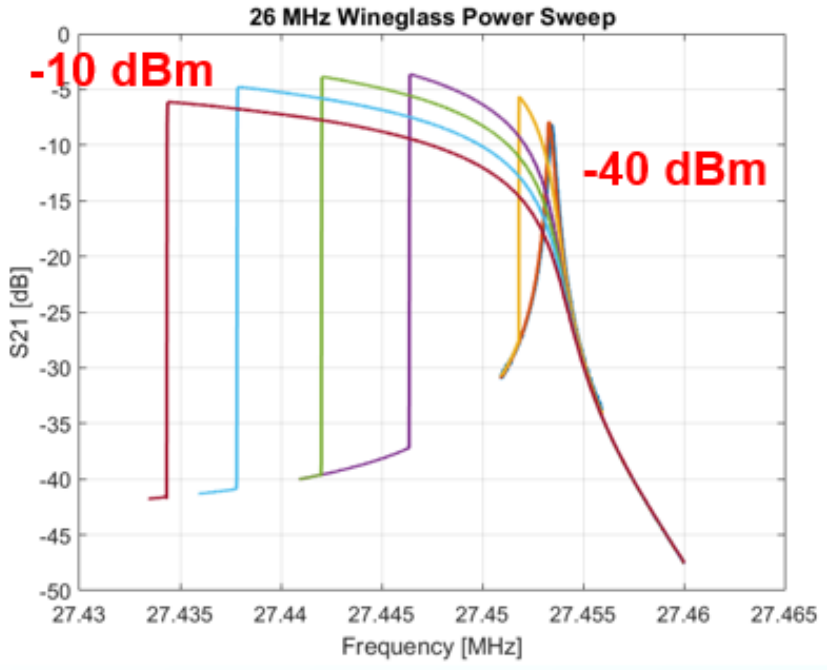

Figure 16: Frequency response of a 40 nm gap 27 MHz wineglass disk resonator, with V_P = 3 V, sweeping input power from -40 dBm to -10 dBm

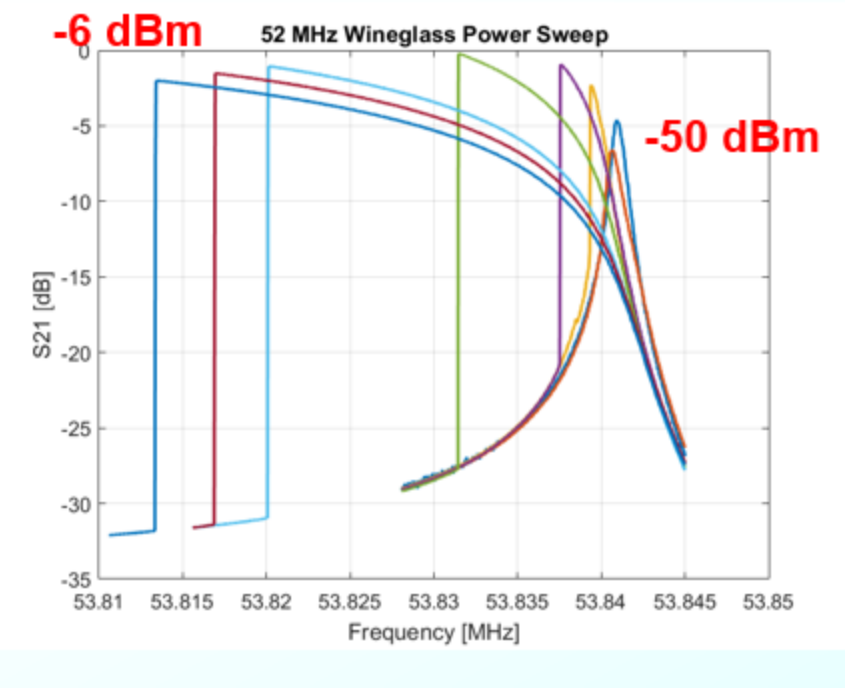

Figure 17: Frequency response of a 40 nm gap 53 MHz wineglass disk resonator, with V_P = 6 V, sweeping input power from -50 dBm to -6 dBm

Chapter 6

Effect of Transducer Nonlinearities on Amplitude Limiting of the Pierce Oscillator

6.1 Theory

As derived in Section 5.1, the series motional resistance of small gap MEMS resonator decreases with increasing amplitude, at least for moderately large amplitudes. In the pierce oscillator, this has a strong impact on the critical g_m for oscillation. Figure 18 shows measurements of a 40 nm gap 53 MHz wineglass disk resonator, along with a finer power sweep at V_P = 7V. The measurement data from Figure 18 was used to generate the R_X versus input amplitude plot in Figure 19, along with the theoretical $g_{m,crit}$ versus input amplitude due to R_X changing. From the measurement, we can see that the variation in $g_{m,crit}$ is fairly significant, dropping by 30% from the small signal value.

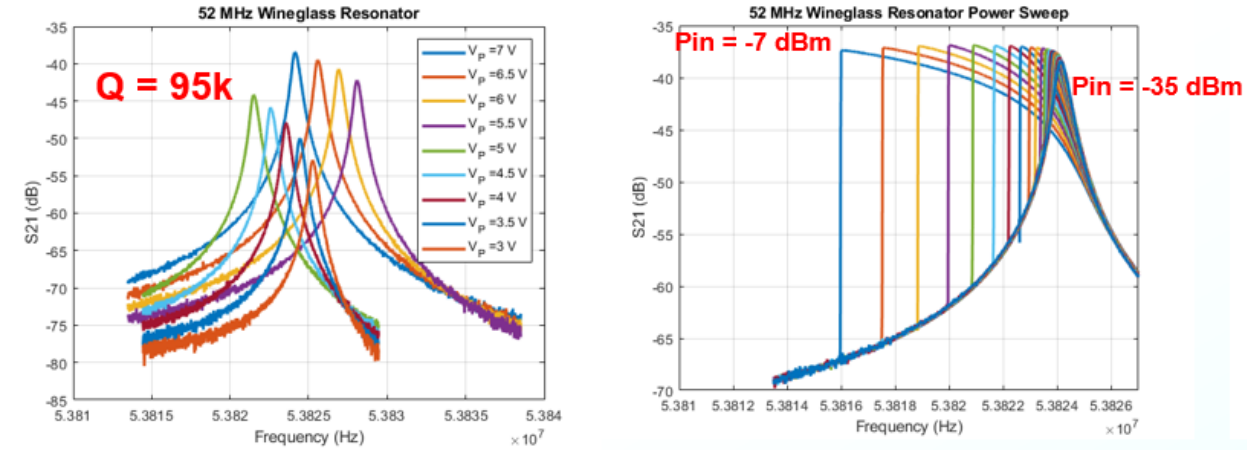

Figure 18: Measurements of a 40 nm gap 53 MHz wineglass disk resonator, sweeping V_P (left) and input power with V_P = 7 V (right)

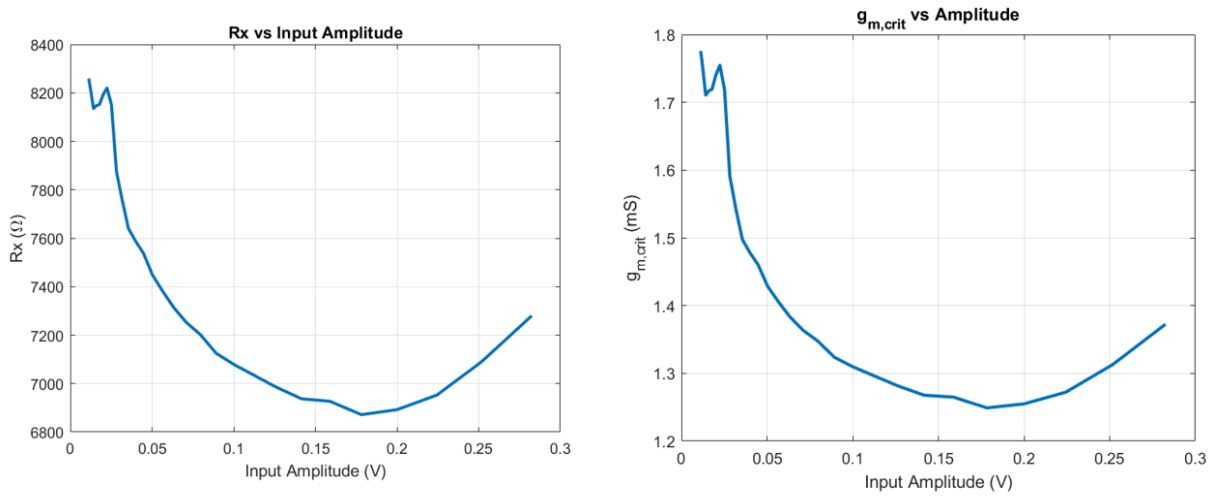

Figure 19: R_X (left) and $g_{m,crit}$ in a pierce oscillator (right) versus voltage amplitude across the resonator port

The result of $g_{m,crit}$ depending on amplitude is hysteresis in the amplitude limiting of the pierce oscillator versus the bias point of the pierce. Figure 20 illustrates a hypothetical example to explain why. The initial oscillation startup occurs at point A, when the small signal g_m of the pierce reaches small signal $g_{m,crit}$. As the amplitude of oscillation increases slightly from startup, the large signal G_m decreases, analyzed in Section 3, but $g_{m,crit}$ decreases due to the R_X nonlinearity of the resonator. This makes point A unstable, making the oscillator jump to point B, where the $g_{m,crit}$ intersects with G_m a second time. From point B, the amplitude can be reduced by decreasing the bias current to reach point C, operating at the intersection of the new G_m curve and $g_{m,crit}$. Note that point C is not reachable from regular oscillation startup, because the small signal g_m of the pierce is not large enough to start oscillation at small signal. The resonator R_X nonlinearity benefits the power consumption of an oscillator, since the steady state operating point of R_X is smaller than the initial small signal value.

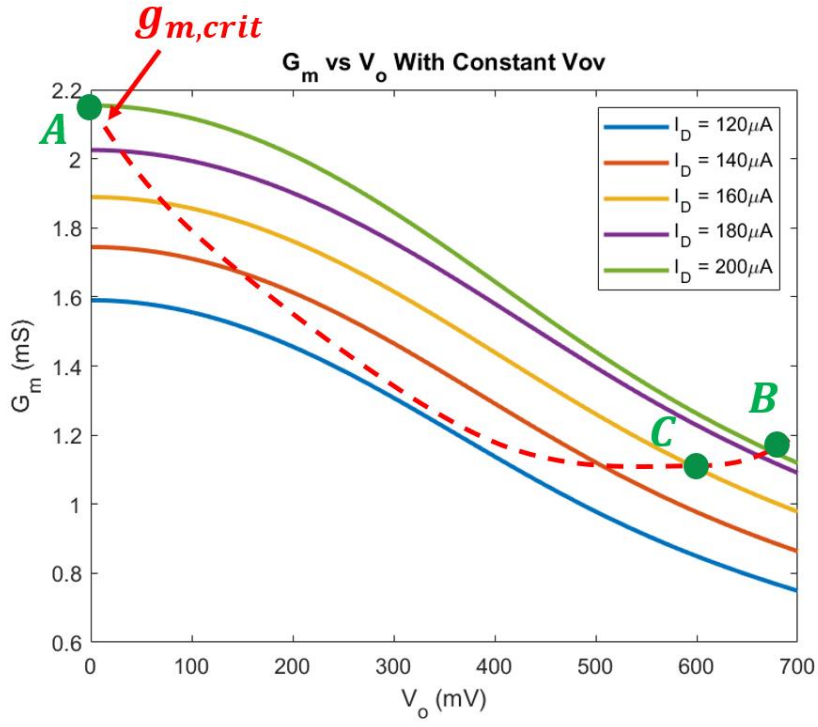

Figure 20: Hypothetical example to demonstrate hysteresis in amplitude limiting of the pierce

6.2 Measurements

The resonator measured in Figure 18 was wire bonded to the pierce sustaining amplifier designed in Section 2. Figure 21 shows the output waveforms and spectrum of the oscillator. From Figure 22, we can see the hysteresis behavior of the amplitude limiting. Instead of gradually increasing with bias current like a crystal oscillator, the amplitude jumps to several hundred millivolts, shown in the forward sweeps in Figure 21. While oscillation is sustained, the amplitude can be adjusted gradually to a desired operating point. Due to the gain expansion of the resonator, the oscillator consumes less power to operate at larger amplitudes, which is a benefit of transducer nonlinearity from shrinking the gap.

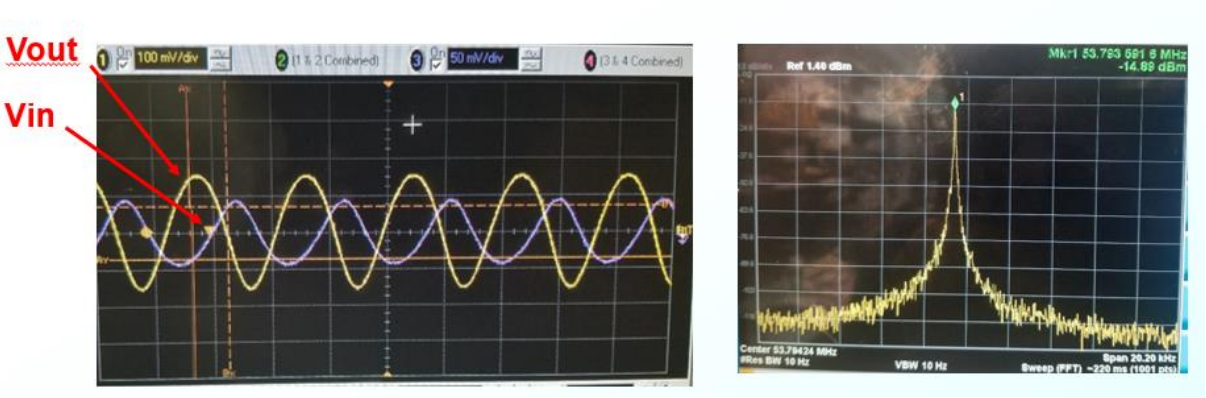

Figure 21: Time domain waveforms (left) and output spectrum of the 53 MHz pierce oscillator

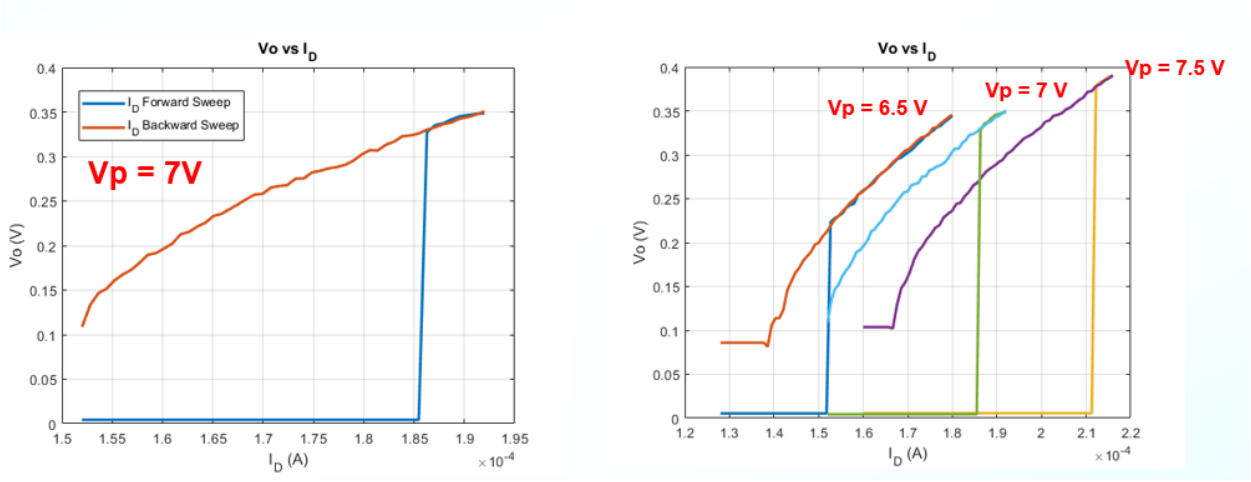

Figure 22: Amplitude limiting of the 53 MHz pierce oscillator versus bias current.

Conclusion

This work demonstrated the difference in amplitude limiting between small gap MEMS and crystal-based oscillators. The analysis gives a possible explanation behind the reduction of R_X of MEMS resonators at higher amplitudes, and how it results in hysteresis in the amplitude limiting of oscillators. For moderately large amplitudes, the nonlinear frequency response of MEMS resonators behaved as the theory predicted, duffing via spring softening, and decreasing R_X with increasing amplitude. At larger amplitudes however, the gain expansion of the frequency response reverses to gain compression, as R_X begin to increase past a certain point. One possibility is mechanical based nonlinearities coming into play, which result in increasing R_X against the transducer gain expansion. Future work would investigate the source of this nonlinearity, and verify the result by matching measurements to predictions. The benefit of having transducer nonlinearities is lower power consumption for oscillators, compared to the nominal linear case. As studied in previous work, the dynamic nonlinearity in MEMS resonators have a negative impact on close to carrier phase noise performance, which is a topic related to this work.

References

[1] T. L. Naing, T. O. Rocheleau, E. Alon and C. T. . -C. Nguyen, "Low-Power MEMS-Based Pierce Oscillator Using a 61-MHz Capacitive-Gap Disk Resonator," in IEEE Transactions on Ultrasonics, Ferroelectrics, and Frequency Control, vol. 67, no. 7, pp. 1377-1391, July 2020, doi: 10.1109/TUFFC.2020.2969530.

[2] Q. Xie, S. Afshar, A. Ozgurluk and C. T. . -C. Nguyen, "199-MHz Polysilicon Micromechanical Disk Array-Composite Oscillator," 2020 Joint Conference of the IEEE International Frequency Control Symposium and International Symposium on Applications of Ferroelectrics (IFCS-ISAF), 2020, pp. 1-5, doi: 10.1109/IFCS-ISAF41089.2020.9234862.

[3] M. Akgul, L. Wu, Z. Ren and C. T. -. Nguyen, "A negative-capacitance equivalent circuit model for parallel-plate capacitive-gap-transduced micromechanical resonators," in IEEE Transactions on Ultrasonics, Ferroelectrics, and Frequency Control, vol. 61, no. 5, pp. 849-869, May 2014, doi: 10.1109/TUFFC.2014.2976.

[4] C. T.-C. Nguyen, “Micromechanical Signal Processors,” Ph.D. Dissertation, Dept, of EECS, University of California at Berkeley, Dec. 1994.

[5] S. Lee, and C. T.-C. Nguyen, "Influence of automatic level control on micromechanical resonator oscillator phase noise," Proceedings of 2003 IEEE Frequency Control Symposium, Tampa, Florida, pp.341-349, May 5-8, 2003.

[6] Wang, Xiaoyu and Amir Mortazawi. “Bandwidth Enhancement of RF Resonators Using Duffing Nonlinear Resonance for Wireless Power Applications.” *IEEE Transactions on Microwave Theory and Techniques* 64 (2016): 3695-3702.